PAPER

In situ rheological monitoring of diffusion-controlled hydrogel crosslinking for embedded 3D bioprinting

Biofabrication

PAPER

RECEIVED
27 March 2026

REVISED
26 May 2026

ACCEPTED FOR PUBLICATION
17 June 2026

PUBLISHED
1 July 2026

In situ rheological monitoring of diffusion-controlled hydrogel crosslinking for embedded 3D bioprinting

Fotis Christakopoulos[1,6], Audrey Shih[2,6], Stella J Chung[2], Carla Huerta-López[1], Lucia G Brunel[2], Narelli de Paiva Narciso[1], Clélia Messin-Roizard[1], Junyi Tao[3], David Myung[2,4,5], Sarah C Heilshorn[1] and Gerald G Fuller[2,*]

[1] Department of Materials Science and Engineering, Stanford University, Stanford, CA, United States of America
[2] Department of Chemical Engineering, Stanford University, Stanford, CA, United States of America
[3] Department of Mechanical Engineering, The University of Tokyo, Tokyo, Japan
[4] Department of Ophthalmology, Byers Eye Institute, Stanford University School of Medicine, Palo Alto, CA, United States of America
[5] VA Palo Alto Healthcare System, Palo Alto, CA, United States of America
[6] Contributed equally to this work.
[*] Author to whom any correspondence should be addressed.

E-mail: ggf@stanford.edu

Keywords: diffusion-enabled bioprinting, dynamic covalent crosslinking, embedded 3D printing, collagen, dynamic hydrogels, corneal epithelial cells

Supplementary material for this article is available online

Abstract

In embedded 3D bioprinting, biomaterial inks are extruded into sacrificial support baths to facilitate the fabrication of complex shapes, even from soft, liquid-like materials. Post-printing, the diffusion of small molecules into or out of the support bath can facilitate ink crosslinking to stabilize the printed structure. In these coupled reaction-diffusion systems, the rheological properties of the ink will change over time. Despite the importance of tuning the mechanical properties of these inks for biological applications, there are currently no methods to accurately predict ink stiffness over time throughout the crosslinking process. Here, we use a custom-developed magnetic stress rheometer to continuously monitor diffusion-driven crosslinking *in situ*. Our approach reveals how gelation kinetics depend on the thickness of the ink layer, and enables predictive estimation of mechanical evolution in these reaction- and diffusion-driven systems. With these insights, we fabricate specimens with predetermined mechanical properties and observe changes in cell phenotype as a response. These insights help inform the design of inks and timing of bioprinting protocols to achieve prints with desirable mechanical properties and further allow the fabrication of prints with patterned mechanical properties.

1. Introduction

The growing gap between organ donor availability and patient demand has driven the development of alternative strategies for tissue repair and transplantation [1]. 3D bioprinting is a rapidly advancing additive manufacturing technique that enables precise patterning of cell-laden inks into complex, tissue-like structures [2, 3]. To fabricate free-standing structures using 3D bioprinting in air, the extruded ink typically needs to have high viscosity and stiffness to retain its structural fidelity both during and post-printing [4]. However, typically softer materials have been found to have increased cytocompatibility [5, 6]. The need for soft biomaterial inks that also resist collapse during and after printing has driven the development of techniques that enable the use of a broad range materials as biomaterial inks by leveraging post-printing, biocompatible, crosslinking strategies [4]. Common approaches involve the bioprinting of a soft, ink material into a shear-thinning support bath that is removed after the post-printing crosslinking step through a thermoreversible phase transition, [7] physical separation, [8–11], or dissolution [12–14] to extract the crosslinked print [4]. The support bath provides

temporary mechanical confinement to the ink during printing, enabling high-fidelity deposition of structurally weak or liquid-like biomaterials [15–17].

Early examples of this embedded bioprinting approach utilized photopolymerization or a thermoreversible or pH-triggered phase transition to induce crosslinking of the ink materials [18–21]. More recently, inks have been designed to crosslink in response to diffusion-mediated reactions. This crosslinking can be accomplished in two different ways, either by diffusion of small molecule crosslinkers from the support bath into the printed filament (diffusion-in) or by diffusion of small molecule competitors, that suppress crosslinking prior to filament deposition, from the printed filament into the support bath (diffusion-out) [22–24]. Crosslinking through photopolymerization or an environmentally-triggered phase transition is typically fast (i.e. less than one min), and the resulting crosslinking process can be accurately modeled on a conventional shear rheometer. However, for systems that rely on diffusion-driven crosslinking, the crosslinking process is slower (i.e. typically greater than 10 min) and inherently challenging to characterize through bulk rheology measurements. This is true even for ink systems that rely on small crosslinkers with high diffusivity, such as calcium ions that diffuse into printed alginate structures [25, 26]. Traditional rheology instruments cannot accommodate *in situ* diffusion between two distinct materials during measurements without mixing them. Moreover, in diffusion-enabled bioprinting, the rheological properties of the final construct depend on the extent of the reaction, which is determined by the diffusion and reaction kinetics and the total residence time of the printed ink in the support bath. Typically the reaction is terminated by removing the construct from the support bath, making the timing of support bath removal critical, yet under studied. Prolonged residence times can be detrimental for cell-laden inks, since suboptimal conditions may compromise cell viability. On the other hand, insufficient residence times can result in insufficient crosslinking and heterogeneous mechanical properties in the printed filament. Currently, the residence time is usually estimated from simplified systems, such as premixed crosslinkers or the exclusion of competitors in diffusion-in and diffusion-out strategies, respectively. These approaches do not account for the role of diffusion and consequently, these predictions may overestimate the extent of crosslinking and stiffness of the printed specimen. More recently, modeling of the diffusive reaction-front with experimentally determined diffusivity values has allowed prediction of the resulting construct mechanical properties and geometries [26, 27]. Moreover, we hypothesize that accurate control over crosslinkin kinetics could allow for the fabrication of specimens with more complex patterns of mechanical properties, since the print path can be designed to achieve different residence times for different regions of the construct. Thus, we seek to further develop a methodology to characterize gelation kinetics in order to optimize residence time in diffusion-based embedded bioprinting. To achieve this we use magnetic rheometry, a technology that previously has been demonstrated to characterize natural and synthetic biomaterials, including abscess fluids, [28] mucus, [29] and hydrogels [30, 31].

Here, we present the addition of a dual-layer setup to our custom-made magnetic stress rheometer (MSR, figure 1(a)) that facilitates direct contact between the ink and the support bath, maintaining continuous diffusion throughout the measurement. The experimental setup imitates an ink filament with a diameter L printed into a support bath (figure 1(b)). This strategy enables continuous, nondestructive shear measurements of an ink layer of thickness L on top of a support bath layer using a small magnetic probe at the surface of the ink layer to monitor diffusion-driven crosslinking *in situ* (figures 1(c) and (d)). With this dual-layer setup, we can predict the extent of crosslinking in the part of the printed filament that is furthest away from the diffusion interface for both diffusion-in (figure 1(c)) and diffusion-out (figure 1(d)) systems. As a model diffusion-in system, we use an ink comprising azide-modified collagen that is crosslinked through a bioorthogonal strain-promoted azide-alkyne cycloaddition (SPAAC) click reaction, with crosslinker molecules diffusing from the support bath into the printed filament (figure 1(c)) [22, 32–35]. For the diffusion-out system, we use polyethylene glycol (PEG)-based inks functionalized with aldehyde (PEG-ALD) and hydrazine (PEG-HYD) groups that form dynamic covalent hydrazone bonds (figure 1(d)) [36, 37]. To tune gelation, a non-toxic competitor molecule is added to the ink to temporarily suppress crosslinking by reversibly reacting with aldehyde groups, keeping the ink extrudable during printing [38, 39]. After printing, the competitor diffuses out of the printed filament into the support bath, allowing the PEG-ALD and PEG-HYD to crosslink [23].

Finally, to demonstrate how this methodology can be used to design bioprinting processes, we use the parameters extracted from these rheological measurements, to fabricate a printed specimen with alternating regions with stiffer and weaker mechanical properties. When used as a scaffold for human corneal epithelial cells (CECs), we observe stereotypical phenotypic mechanosignaling responses, highlighting the critical importance of controlling the final construct mechanical properties during bioprinting. Taken together, this work presents a method to follow the temporal evolution of diffusion-enabled inks commonly used in embedded 3D bioprinting to inform the design of printing protocols for the

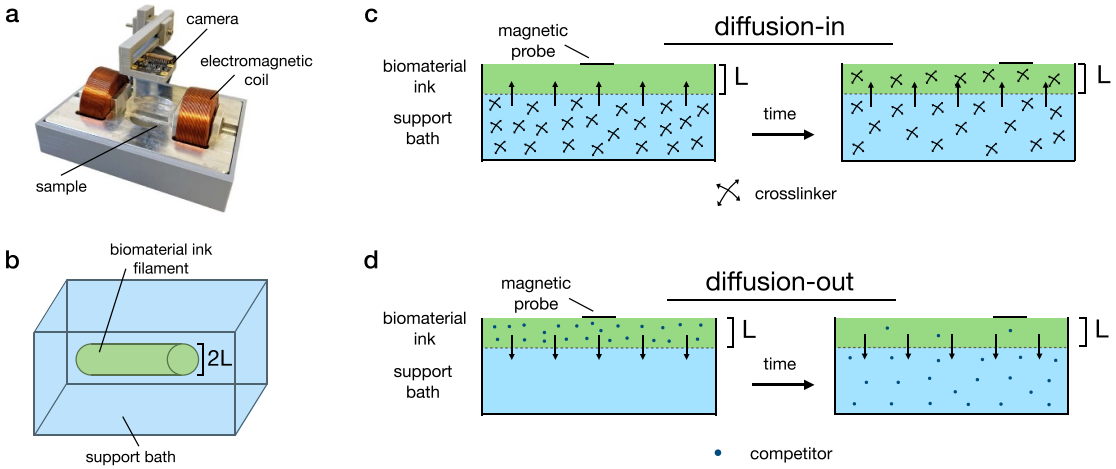

Figure 1. Overview of characterization methodology. (a) The magnetic stress rheometer (MSR) has a pair of electromagnetic coils that drive the magnetic probe to move laterally across the surface of the ink. A camera captures the motion of the probe, which is used to calculate strain, γ, and consequently creep compliance, J. (b) Schematic showing a typical diffusion-enabled bioprinting setup, where a filament of ink with radius L is printed into a support bath. (c) and (d) Schematics of the MSR set up for diffusion-in and diffusion-out ink-bath systems, respectively. (c) To mimic diffusion-in bioprinting, a layer of ink with thickness L is placed over a support bath that contains crosslinker molecules, enabling measurements of *in situ* gelation as the molecules diffuse into the ink layer. (d) To mimic diffusion-out bioprinting, a layer of ink with thickness L that contains competitor molecules is layered over the support bath, enabling measurements of *in situ* gelation as the competitor molecules diffuse out of the ink layer.

fabrication of constructs with predictable mechanical properties.

2. Materials and methods

2.1. Ink and support bath preparation

To prepare the collagen ink, type I bovine atelocollagen (Advanced BioMatrix) was modified with azide functional groups [33, 40, 41]. Acidified collagen at a concentration of 10 mg ml^{-1} was neutralized on ice using 1 M sodium hydroxide (NaOH, Sigma-Aldrich) and subsequently ultrapure deionized water (Millipore) and 10X phosphate buffered saline (PBS, Millipore) were added to achieve a final collagen concentration of 8 mg ml^{-1} with a pH of 7.5. Azide functional groups were introduced via N-hydroxysuccinimide (NHS) ester chemistry using azido-PEG$_4$-NHS ester (BroadPharm), which was dissolved in dimethyl sulfoxide (DMSO, Fisher) at 100 mg ml^{-1} and added to the neutralized collagen solution at a 2:1 molar ratio, relative to primary amines, resulting to a degree of functionalization of 50% [41]. The mixture was rotated at 4 °C for 2 h and then dialyzed overnight against 1X PBS at 4 °C using a 3.5 kDa MWCO dialysis cassette (Thermo Scientific). The resulting azide-modified collagen was stored at 4 °C. For the experiments using a lower collagen concentration, the collagen was diluted with 1X PBS. For SPAAC-based crosslinking experiments, a 4-arm PEG with dibenzocyclooctyne end groups (PEG-DBCO, 10 kDa, Creative PEGWorks) was incorporated in the support bath. To prepare the fluorescently-labeled collagen, collagen azide was mixed with 1 wt% AlexaFluor647 NHS ester (Thermo Fisher Scientific) in DMSO and left to react 24 h at 4 °C. Subsequently, the solution was dialyzed against 1X PBS at 4 °C for 3 days using a 7 kDa MWCO dialysis cassette (Thermo Fisher Scientific). For the fluorescently-labeled collagen prints, non-labeled collagen azide was mixed with the fluorescently-labeled collagen azide at a ratio of 20:1.

To prepare the dynamic hydrazone PEG hydrogels, 4-arm PEG-aldehyde (PEG-ALD, 20 kDa, Creative PEGWorks) and 4-arm PEG-hydrazine (PEG-HYD, 20 kDa, Creative PEGWorks) were each dissolved at 16 wt% in 1X PBS. The competitor (hydrazinoacetic acid, Sigma-Aldrich) was also dissolved in 1X PBS and neutralized to pH 7.5 using 1 M NaOH. The competitor stock was then mixed with the PEG-HYD solution since they are nonreactive with each other. PEG-ALD was added in last to reach a final concentration of 8 wt% PEG-ALD, 8 wt% PEG-HYD, and 10 mM competitor, unless stated otherwise.

A commercial gelatin microparticle support bath was used (LifeSupport, FluidForm Inc.), and prepared following the instructions of the manufacturer. Briefly, lyophilized LifeSupport was hydrated with cold 1X PBS for 10 min at a concentration of 50 mg ml^{-1} and subsequently centrifuged at 2000 rcf for 5 min and the supernatant was removed via aspiration. For the diffuse-in experiments the hydrated LifeSupport was first centrifuged at 1500 rcf for 5 min

and the supernatant was aspirated. Subsequently, 1 ml of PEG-DBCO dissolved in 1X PBS was mixed into the slurry (final PEG-DBCO concentration of 3 mg ml^{-1}) and centrifuged at 2000 rcf for 5 min as described previously.

2.2. Diffusivity measurements

The diffusivity of the small molecule crosslinker through the support bath, uncrosslinked collagen, and fully crosslinked collagen was determined using fluorescence recovery after photobleaching (FRAP). A 10 kDa FITC-dextran probe (Sigma) was used and five replicates of each condition were tested by loading 30 μL of material for each replicate into a clear-bottom, half-area 96-well plate (Greiner Bio-One). FRAP experiments were performed using a STELLARIS 5 confocal microscope (Leica) with 60 s of photobleaching (110 μm $\times$ 110 μm, 488 nm laser, 100% intensity) followed by 90 s of acquisition time. Diffusion coefficients were calculated using the 'frap analysis' MATLAB program [42].

2.3. Bulk rheometry

Small-amplitude oscillatory shear (SAOS) measurements were conducted on a Discovery Hybrid rheometer (DHR-3, TA Instruments, New Castle, DE) with a 2° cone-and-plate geometry and a solvent trap to prevent evaporation. Time sweep measurements to follow the gelation of the different premixed inks were carried out at an angular frequency of 1 rad s^{-1} and a shear strain amplitude of 1%. Frequency sweeps were conducted at a shear strain amplitude of 1%, in the linear viscoelastic regime. Stress-ramp measurements at an angular frequency of 10 rad s^{-1} and rotational measurements of the support bath material were conducted on an AR-G2 rheometer (TA Instruments, New Castle, DE) with a 40 mm parallel plate geometry and a measuring gap of 0.8 mm.

2.4. Magnetic stress rheometry

The custom-built MSR was used to characterize the temporal evolution of the viscoelastic properties of the two biomaterial inks throughout diffusion-mediated crosslinking. Briefly, the instrument uses a flat rectangular magnetic probe with a length of 6 mm and width of 2 mm that rests on the surface of the ink layer, suspended by surface tension. Electromagnetic coils positioned on both sides of the material container generate a magnetic field gradient that applies shear stress to the probe, inducing translational motion along its long axis. A camera mounted above the sample records the probe displacement at 30 frames per second and current data from the coils is simultaneously recorded with a Raspberry Pi. The motion of the probe is tracked from the videos with a custom MATLAB script, providing strain data, while the current signal provides stress data via a force calibration procedure as described in Shih *et al* [28]. Prior studies have confirmed that MSR measurements agree with standard CSR rheometry for bulk viscoelastic materials without interfacial contributions [28]. The rheometer setup is shown in figure 1(a). All measurements were conducted at room temperature to reflect typical bioprinting conditions. The setup was enclosed in an environmentally controlled chamber maintained at 90% humidity to prevent evaporation effects during the measurements. Measurements conducted on the custom-build MSR are referred to as MSR measurements in the rest of the study.

2.5. Dual-layer setup

Samples were placed in custom-fabricated rectangular plexiglass containers with dimensions of 32 mm (length)$\times$7 mm (width)$\times$10 mm (height). The support bath was first extruded into the container and centrifuged (4120 rcf for 10 min) to remove air pockets and ensure uniformity in support bath density. Excess support bath material was then leveled using custom 3D-printed doctor blades designed to produce defined thicknesses. To approximate Couette flow conditions, the thicknesses of the ink layers were chosen to be $\leqslant$ 2 mm, matching the width of the probe along its non-translating axis. This range of length scales also matches common ranges of filament diameters [43–45]. Biomaterial ink was subsequently deposited on top to fill the upper layer to the brim of the container with a pipette. The magnetic probe was placed on the surface with plastic tweezers and rheological measurements on the MSR were initiated immediately. As the measurements take place at the ink-air interface, sources of error may include edge effects, temperature variability, and humidity variability. To try to minimize these impacts, we perform measurements within a humidity and temperature controlled chamber. For the diffusion-in system, control experiments include reaction-only, where PEG-DBCO is additionally pre-mixed in the collagen ink, and no crosslinking, where PEG-DBCO is not added in the support bath. For the diffusion-out system, control experiments include reaction-only, where no competitor molecules are added in the PEG ink, and no crosslinking, where competitor molecule is also added in the support bath. The control measurements were conducted with an ink layer thickness of 1 mm.

2.6. Creep compliance

For the creep compliance measurements, a constant magnetic force of τ_0 was applied to the probe for 10 s, followed by a recovery period of 30 s to allow the sample to relax. This 40-s cycle was repeated in both directions and averaged to generate a single displacement curve. A custom MATLAB script was used to analyze the video data and determine the displacement

of the probe over time. The strain (γ) was then calculated from the displacement (x) through $\gamma = x/L$, where L is the thickness of the ink layer. The applied stress (τ_0) was calculated through $\tau_0 = F/A$, where the applied force F is estimated by collecting current readout data over time $I(t)$ from the Raspberry Pi that are related to F by a scaling factor, described by calibration experiments from our previous work, [28] and A corresponds to the area of the probe. In this work, the applied stresses τ_0 ranged from 0.08 to 0.83 Pa. The creep compliance curves were calculated by $J = \gamma/\tau_0$. Creep compliance measurements were repeated every few minutes over the course of several hours, until the displacement of the probe could not be discerned in the video data. Example data of the dynamic PEG ink showing each creep compliance measurement across the x-axis and the evolution of these curves over the crosslinking duration on the y-axis is presented in supplemental figure S2(a). The shape of the curves changes over time, during crosslinking, from a liquid-like response with gradual and partial viscoelastic recovery to a solid-like response with immediate and full recovery as shown in a two-dimensional projection of the curves on a log-y axis (supplemental figure S2(b)).

2.7. Parameter calculation

In creep experiments, zero-shear viscosity (η_0) and steady-state compliance (J_s^0) are commonly reported as analogs to loss and storage terms, describing the resistance to flow and the softness of the material, respectively [46]. Here, we report the inverse of steady-state compliance ($1/J_s^0$) to provide an effective modulus. These two parameters were calculated by fitting each creep compliance curve to a 5-element Kelvin–Voigt model, as described in equation 1:

$$J(t) = \begin{cases} \frac{t}{\eta_0} + \frac{1}{G_1}\left[1 - \exp\left(\frac{-G_1 t}{\eta_1}\right)\right] + \frac{1}{G_2}\left[1 - \exp\left(\frac{-G_2 t}{\eta_2}\right)\right], & t \leqslant t' \quad (1a) \\ \frac{t'}{\eta_0} - \frac{1}{G_1}\left[\exp\left(\frac{-G_1 t'}{\eta_1}\right) - \exp\left(\frac{-G_1 (t-t')}{\eta_1}\right)\right] & \\ \quad - \frac{1}{G_2}\left[\exp\left(\frac{-G_2 t'}{\eta_2}\right) - \exp\left(\frac{-G_2 (t-t')}{\eta_2}\right)\right], & t > t', \quad (1b) \end{cases}$$

where t' corresponds to the duration of the applied stress during the creep experiment. The role of each element in the model in a compliance curve is shown in supplemental figure S3. Our prior work has shown that the dominant relaxation timescales in polymeric materials can be sufficiently captured with just the recovery phase [28]. Thus, the recovery phase of each compliance curve was fitted to equation 1(b) to extract η_0, G_1, and G_2. From that, the steady-state compliance is calculated through: $J_s^0 = 1/G_1 + 1/G_2$. Over the duration of crosslinking, η_0 and $1/J_s^0$ were calculated for each creep experiment mapping out the evolution of viscoelastic properties throughout gelation.

2.8. Validation experiments

Control experiments were performed to validate the measurements by the MSR. A non-gelling solution of 40 wt% 20 kDa PEG was used as a negative control. The MSR-measured η_0 and $1/J_s^0$ are shown in supplemental figure S4(a). The bulk rheometry measured viscosity was averaged across a frequency from 0.1 s^{-1} to 200 s^{-1} (red doted line, supplemental figure S4(a)) and compared to the viscosity measured through the MSR over 400 min, showing excellent agreement with each other. Moreover, the rheological properties remain generally constant over the duration of the MSR measurements, indicating that evaporation effects are minimal.

To confirm the ability of the MSR to capture gelation kinetics, the crosslinking of gelatin was characterized. A thermoreversible 3% gelatin solution was heated to 37 °C to reach a fully liquid state before being placed on the MSR for immediate measurement. The entire MSR was placed on ice to allow the gelatin to crosslink. The rheological parameters (η_0 and $1/J_s^0$) measured by the MSR are presented in supplemental figure S4(b) and show significant stiffening compared to the non-gelling PEG solution.

2.9. 3D printing

A custom-built dual extruder print, adapted from a MakerGear M2 Rev E plastic 3D printer, was used for the 3D printing experiments as described earlier [22, 23, 47]. The printing was performed with a 17G blunt needle ($d = 1.067$ mm), at room temperature, and at a printing speed of 1 mm s^{-1} in a sterile tissue culture cabinet.

2.10. Cell culture

Human telomerase immortalized corneal epithelial cells (CECs, ATCC CRL-11 135) were kindly donated by Dr Ali Djalilian (University of Illinois at Chicago, USA). CEC growth medium was prepared with keratinocyte SFM cell medium (Gibco, 17 005 042) supplemented with 100X penicillin-streptomycin (Gibco, 15 140 122), 200X hydrocortisone (STEMCELL Technologies, 07 925),

and 2000X insulin (Sigma- Aldrich, I9278). Before plating the cells, standard cell culture flasks were coated with FNC Coating Mix (Athena Enzyme Systems, 0407 H) for 3 min at room temperature and excess FNC was removed from the flasks. Cells were maintained at sub-confluency, and medium was changed every 2 to 3 days. CECs were passaged upon reaching 80% confluency. For cell mechanobiology experiments, cells were seeded at a density of 10 000 cells cm^{-2} on hydrogel surfaces and were cultured for 24 h in complete media before being processed.

2.11. *In vitro* characterization

Cells were washed three times with PBS and fixed with 4% paraformaldehyde (Thermo Scientific, 28 908) at RT for 30 min. Cells were then washed three times with PBS and permeabilized with 0.25% (v/v) Triton X-100 (Sigma-Aldrich, T8787) in PBS (PBS-T) for 1 h at room temperature with gentle rocking. Samples were blocked with 5% (w/v) bovine serum albumin (Sigma-Aldrich, A9647), 5% (v/v) goat serum (Gibco, 16 210 064), and 0.5% Triton X-100 in PBS for 3 h at room temperature with gentle rocking. Antibodies were diluted in antibody dilution solution, which consisted of 2.5% (w/v) bovine serum albumin (BSA), 2.5% (v/v) goat serum, and 0.5% Triton X-100 in PBS. Immunostaining with anti-YAP antibody took place at 4 °C overnight with gentle rocking. After incubation with primary antibody, samples were washed three times with PBS-T for 30 min each. Secondary antibody, phalloidin, and 4',6-diamidino-2-phenylindole (DAPI) were also incubated at 4 °C overnight with gentle rocking. The following antibodies/reagents were used at the indicated dilutions: rabbit anti-YAP antibody (1:200, Invitrogen, PA1-46 189), DAPI (1 μg ml^{-1}, Cell Signaling, 4083 s), goat anti-rabbit Alexa Fluor 488 (1:500, Invitrogen, A-11 008), and Alexa Fluor 647 phalloidin (1:250, Invitrogen, A22287). Next, cells were washed three times with PBS-T for 20 min each and then mounted onto no. 1 coverslips with Fluoromont G (Thermo Fisher, 00-4958-02). After curing for 24 h, tilescan images of the printed samples were acquired with a fluorescent microscope (Keyence, BZ-X1000 series) using a 10X air objective. Subsequently, samples were imaged with a confocal microscope (Leica SPE, Las-X software) using a 40X (1.4 NA) oil objective. ImageJ was used to segment the outer membrane of cells and compute total cell area. DAPI staining was used to quantify nuclei. Only particles with an area higher than 50 μm^2 were analyzed. Data presented in the figures represent independent experimental replicates. Measurements are reported as mean ± standard deviation (SD). Statistical analyses were performed using GraphPad Prism. Normality of data distribution was assessed using the Shapiro–Wilk test. Differences between groups were evaluated using an unpaired Student's t-test for normally distributed data or a Mann–Whitney U test for non-normally distributed data. Statistical significance was defined as follows: not significant (ns), * $p < 0.05$, *** $p < 0.001$, and **** $p < 0.0001$.

3. Results and discussion

3.1. Selection of polymer backbone concentration for diffusion-in bioprinting model

We first explored the range of biomaterial ink formulations that would result in constructs with biologically relevant mechanical properties. For many soft tissue models, weak gels with shear storage moduli (G') less than ≈1 kPa commonly promote the most physiological cell phenotypes [41, 48–50]. The final stiffness of the hydrogel is a consequence of the final concentration of crosslinks, which depends both on the concentration of polymer backbone and the concentration of crosslinker. In diffusion-in bioprinting, the crosslinker concentration is constantly changing as the crosslinker diffuses from the support bath into the biomaterial ink and then reacts with functional groups on the polymer backbone. To reduce this coupled reaction-diffusion system to a reaction-only system, we first evaluated the time-dependent rheology of biomaterial inks that had been pre-mixed with a known concentration of crosslinker (figure 2(a)).

With conventional bulk shear rheology, we measured the time evolution of the storage (G') and loss (G'') moduli of collagen-azide inks with concentrations of 2, 4, and 6 mg ml^{-1}, each with 3 mg ml^{-1} of the 4-arm PEG-DBCO crosslinker. This results in final formulations with stoichiometric ratios between the azide and cyclooctyne functional groups of 1:3.6, 1:1.8, and 1:0.9, respectively, allowing us to monitor the reaction kinetics without diffusional contributions. As expected, the onset of the sol-gel transition (as indicated by the crossover between G' and G'') was faster for the higher collagen concentrations (figure 2(b)). The 2, 4, and 6 mg ml^{-1} formulations had gelation times of 2.4, 3.5, and 4.3 min, respectively. Also as expected, increasing the collagen concentration resulted in stiffer final gels, as indicated by the plateau shear storage moduli of 175, 480, and 890 Pa, respectively. This is presumably due to both the higher polymer volume fraction and more effective crosslinking when the stoichiometric ratio of the reactants is close to the ideal ratio of 1:1 [51–53].

We next compared these bulk measurements of the biomaterial ink with characterization performed on our magnetic stress rheometry system, which has a bilayer setup that includes both a biomaterial ink and a support bath (figure 2(a)). Specifically, in this

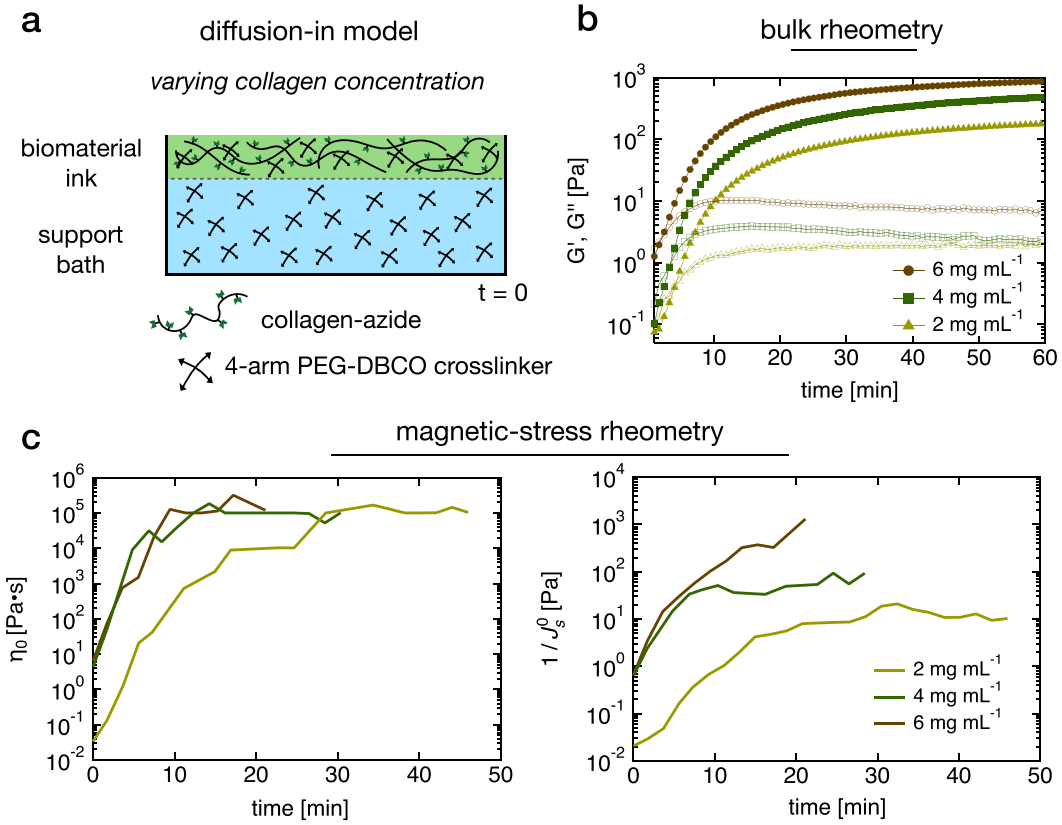

Figure 2. Gelation curves over time for collagen inks with varying polymer backbone concentration. (a) Schematic of the magnetic stress rheology setup and ink and support bath materials used for the diffusion-in model. (b) Bulk rheology measurements of the temporal evolution of storage (filled symbols) and loss (open symbols) moduli for inks containing 2, 4, and 6 mg ml^{-1} of collagen premixed with 3 mg ml^{-1} of the crosslinker. No support bath is present. (c) Magnetic stress rheology measurements of the temporal evolution of η_0 (left) and $1/J_s^0$ (right) for inks containing 2, 4, and 6 mg ml^{-1} of collagen premixed with 3 mg ml^{-1} of the crosslinker. The underlying support bath also included 3 mg ml^{-1} of the crosslinker.

magnetic stress rheometry system, creep measurements are conducted on the surface of the top (biomaterial ink) layer by imaging the motion of a floating magnetic probe exposed to a magnetic field of known strength. As the yield stress of the underlying support bath (100 Pa, supplemental figure S1(b)) is significantly higher compared to the stresses applied during the creep measurements (0.08–0.83 Pa), minimal deformation of the support bath is expected. Thus, the time-dependent motion of the magnetic probe can be analyzed to determine the viscoelastic properties of the biomaterial ink in isolation. This consideration becomes more important at later crosslinking times when higher stress is required to perform the creep measurements due to the increased stiffness of the ink. For this set of experiments, the same concentration of crosslinker (3 mg ml^{-1}) was pre-mixed into both the ink and the support bath to remove diffusional contributions.

In creep experiments, zero-shear viscosity (η_0) and steady-state compliance (J_s^0) are typically reported as analogs to loss (G'') and storage ($G\prime$) terms, describing the resistance to flow and the stiffness of the material, respectively (figure 2(c)) [46]. Similar to the bulk measurements, an increase in collagen concentration lead to faster gelation, as both the η_0 and J_s^0 curves for the 4 mg ml^{-1} ink reach a plateau prior to that of the 2 mg ml^{-1} ink. Moreover, the higher $1/J_s^0$ plateau value of the 4 mg ml^{-1} ink compared to the 2 mg ml^{-1} ink indicates a stiffer final network, consistent with the bulk rheology results. Interestingly, while rheological differences between the 2 and 4 mg ml^{-1} ink formulations were readily apparent in the η_0 curves (figure 2(c), left), the 6 mg ml^{-1} ink had a viscosity-time profile similar to that of the 4 mg ml^{-1} ink. Similarly, in the $1/J_s^0$ curve, the 6 mg ml^{-1} ink did not display a plateau before the maximum stress applied by our current setup was reached (figure 2(c), right). These data indicate that the magnetic field strength of our current setup is appropriate to sensitively capture the full rheological spectrum of materials with a stiffness of up to at least 480 Pa. This sensitivity can be easily tuned for other applications by applying a higher maximum stress through either a stronger magnetic field or a probe with a higher magnetic volume force [28]. Taken together, the bulk and magnetic stress rheometry measurements allowed us to identify the 4 mg ml^{-1} ink formulation as having the aforementioned appropriate stiffness relevant for soft tissue models ($\lesssim$1 kPa) and validated our custom setup as appropriate to measure the time-dependent viscoelastic properties of this chosen ink formulation.

3.2. Quantification of the effective reactant diffusivity for diffusion-in inks

We next modified our experimental setup to initially pre-mix the crosslinker only with the support bath and not the biomaterial ink, thereby introducing time-dependent diffusion into the model. To characterize the role of diffusion length on gelation kinetics, we next measured the viscoelastic properties of collagen inks (4 mg ml^{-1}) with varying ink layer thicknesses L (figure 3(a)) using the MSR. For both η_0 and $1/J_s^0$ (figure 3(b), supplemental figure S5(a)), steeper increases over time are observed for thinner ink layers, indicating faster gelation. This trend demonstrates diffusion-limited crosslinking, where the rate of gelation is dependent on the diffusion layer thickness, as opposed to a simple reaction-governed system. Similar behavior has been previously observed in an alginate ink crosslinked through the diffusion of calcium ions [26]. A larger length (i.e. thickness) delays the transport of crosslinker molecules through the entire ink layer to the top surface (i.e. the center of a printed filament).

The shear modulus, G, of a material varies directly with crosslinking density, ρ_x:

$$G = \frac{nk_BT}{V} = \nu k_BT = \frac{\rho_x RT}{M_c}, \tag{2}$$

where V is the volume, k_B the Boltzmann's constant, T the absolute temperature, n the number of polymer chains, ν number density, and M_c the molecular weight between crosslinks [54, 55]. Since we use the inverse of steady-state compliance $1/J_s^0$ as an analog for G, we use it as a proxy for tracking the extent of crosslinking over time. To quantify the relationship between layer thickness and gelation time, we defined a characteristic diffusion time t_D as the time required to reach 90% of the maximum $log(1/J_s^0)$ for each condition. Dimensional analysis of the definition of diffusivity gives

$$L \propto \sqrt{Dt}. \tag{3}$$

Using this relation, we calculated an effective crosslinking diffusivity D by plotting L^2 against t_D, using a layer thickness of 0 mm for the pre-mixed, reaction-only condition (figure 3(c)). The experimental data resulted in a clear linear fit (R^2 value of 0.929), further supporting the idea of a diffusion-driven gelation mechanism, with the slope estimating the effective crosslinker diffusivity D as 4.97×10^{-3} mm^2 min$^{-1} \approx 82.8$ μm^2 s^{-1}.

To put these results into context, we characterized diffusivity using an alternative procedure: FRAP. Briefly, a 10 kDa fluorescent-dextran probe (similar in size to our PEG-DBCO crosslinker) was pre-mixed with either uncrosslinked collagen ink, crosslinked collagen gel, or the gelatin microparticle support bath (supplemental figure S6). The FRAP-estimated diffusivity for dextran within the collagen ink was $D \approx 65$ μm^2 s^{-1}, with no statistical difference detected between the sol-state and gel-state, indicating minimal changes in diffusivity during the crosslinking procedure for 10 kDa-sized diffusants. Using a similar procedure, the FRAP-estimated diffusivity for the support bath was $D \approx 45$ μm^2 s^{-1}. We noted that the FRAP measurements and rheometry-based estimates of effective diffusivity resulted in values with a similar order of magnitude.

To evaluate whether this biofabrication system is diffusion- or reaction-limited, we calculated the second Damköhler number, Da, a dimensionless parameter that describes the ratio of diffusion time to reaction time [56]:

$$Da = \frac{t_d}{t_r} = \frac{kc_0L^2}{D}. \tag{4}$$

Systems are diffusion-limited for $Da > 1$ and reaction-limited for $Da < 1$. Da was calculated using our rheometry-derived effective crosslinker diffusivity, an initial crosslinker functional arm concentration (c_0) of 1.2 mM, and a reported SPAAC reaction rate (k) of 310 mM^{-1}s^{-1} for azide groups reacting with DBCO [57]. With these parameters, the range of Da spans from 1×10^6 to 1.7×10^7 for the ink layer thicknesses evaluated, indicating that diffusion dominates at the length scales studied (supplemental table S1). The critical thickness L_c at which $Da = 1$ is approximately 0.47 μm. This means that for 3D printing of filaments with diameters larger than 0.94 μm, the extent of crosslinking can be adequately predicted based on diffusion kinetics, while printing protocols for smaller filaments must primarily consider the reaction kinetics. Since the extent of crosslinking is directly related to the final scaffold mechanical properties, consideration of the Da allows for the design of bioprinting processes that have patterned regions of differing stiffness through control of the total reaction-diffusion time.

The higher apparent diffusivity derived from the magnetic rheometry measurements compared to FRAP measurements may arise from the larger radius of gyration of the linear probes typically used in FRAP measurements compared to that of branched polymers of the same M_w, such as the 4-arm crosslinker molecules used here. Furthermore, we point out that the rheometry measurement reports on the effective gradient diffusivity of the crosslinker reaction front as it moves across the ink layer, as inferred by the resulting increase in stiffness. In contrast, no reaction and no diffusant gradients are present in the FRAP measurements. Taken together, these findings highlight how a dual-layer microrheology system can be used to quantitatively evaluate the reaction-diffusion kinetics of diffusion-in ink materials. This analysis can guide the design of bioprinting processes to fabricate structures with predetermined, patterned mechanical properties.

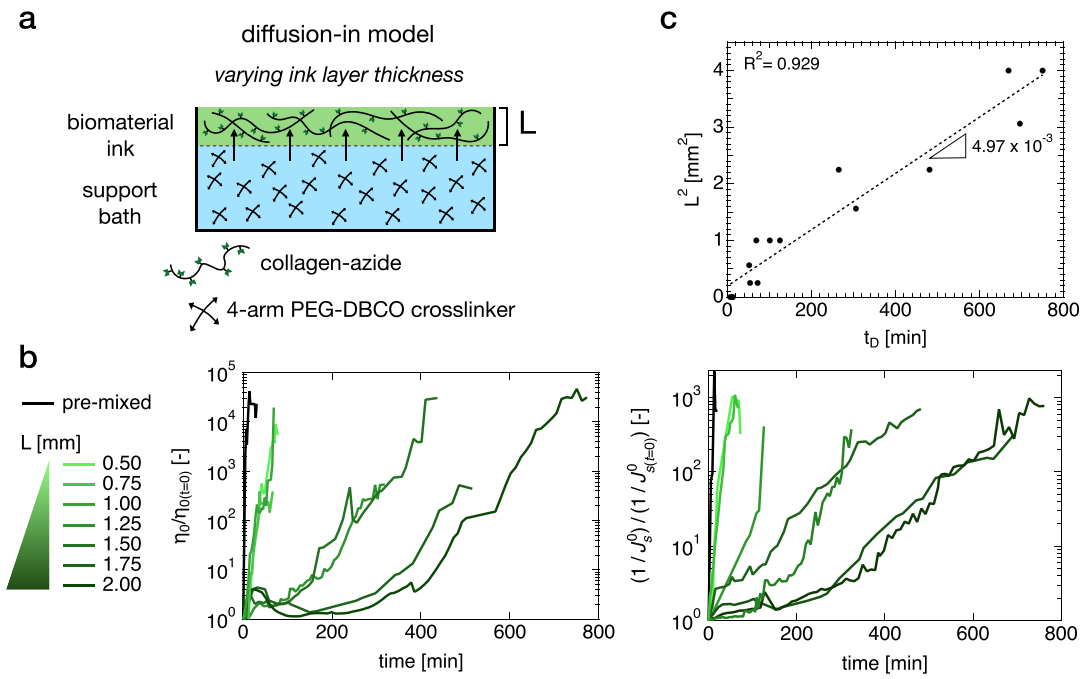

Figure 3. Collagen ink crosslinking dependence on ink layer thickness. (a) Schematic of the experimental setup with crosslinker diffusing from the underlying support bath into the top layer of biomaterial ink, which has different thickness L to mimic different printed filament diameters. (b) Collagen ink crosslinking for the pre-mixed solution (i.e. reaction only) and for different diffusion lengths (ink layer thickness, L) presented in terms of η_0 (left) and $1/J_s^0$ (right), normalized by the initial time point. (c) Correlation between L^2 and diffusion-time t_D with the linear regression (dashed line) having a slope corresponding to diffusivity.

3.3. Quantification of the effective inhibition rate constant for diffusion-out inks

After having examined a diffusion-in system used to enable printing of soft biomaterial inks, we next explored another recently developed, diffusion-enabled bioprinting approach that utilizes a diffusion-out system. The biomaterial ink was a PEG-based hydrogel crosslinked through dynamic covalent chemistry. Specifically aldehyde-modified, 4-arm PEG (PEG-ALD) was mixed with hydrazine-modified, 4-arm PEG (PEG-HYD) to form dynamic hydrazone bond crosslinks. While the hydrogel would not be printable if fully crosslinked, the addition of a small molecule competitor temporarily prevents the formation of some of the crosslinks, lowering the yield stress [23, 38, 58, 59]. Here, the competitor small molecule, hydrazinoacetic acid, is pre-mixed with the ink to compete with PEG-HYD for reaction with PEG-ALD, effectively suppressing gelation until it diffuses out of the ink into the support bath (figure 4(a)). To explore how gelation kinetics can be tuned with small-molecule interactions, we first examined the effect of competitor concentration on the dynamic PEG hydrogel without diffusion using bulk rheological measurements. Bulk rheometry showed that pre-mixing 10 mM competitor with the PEG ink to achieve a stoichiometric ratio of ALD groups to competitor molecules of 1.6:1 completely inhibited gelation (figure 4(b)). The storage modulus, G', remained below the loss modulus, G'', throughout the entire duration of the experiment, and both moduli remained orders of magnitude lower than the uninhibited case without competitor, where gelation occurred after ≈30 min to form a hydrogel with a final stiffness of 1000 Pa. This confirms that the competitor can effectively inhibit the formation of hydrazone bonds between PEG-HYD and PEG-ALD in our model ink system.

We next used magnetic-stress rheometry to monitor the evolution of η_0 and $1/J_s^0$ for 2 mm thick ink layers on top of the support bath in a diffusion-out setup, with varying initial competitor concentration (figure 4(c)). As competitor concentration increases, the gelation process becomes progressively delayed, indicating slower formation of effective hydrazone crosslinks due to competitive inhibition. The characteristic diffusion time t_D (as estimated by the time required to achieve 50% of the maximal stiffness) is found to linearly increase with increasing competitor concentration (figure 4(d)). The linear relationship between competitor concentration and t_D supports a pseudo-first-order kinetic model for competitive inhibition, $t_D = [\text{competitor}]/k_i + t_{D_0}$, where k_i is the effective inhibition rate constant. We note that this k_i is not the reaction rate constant for the aldehyde-hydrazine reaction, but rather k_i is an effective rate constant that describes the time-dependent motion of the competitor as it simultaneously reacts and diffuses through the ink layer. From the slope of the linear regression, we extract an effective inhibition

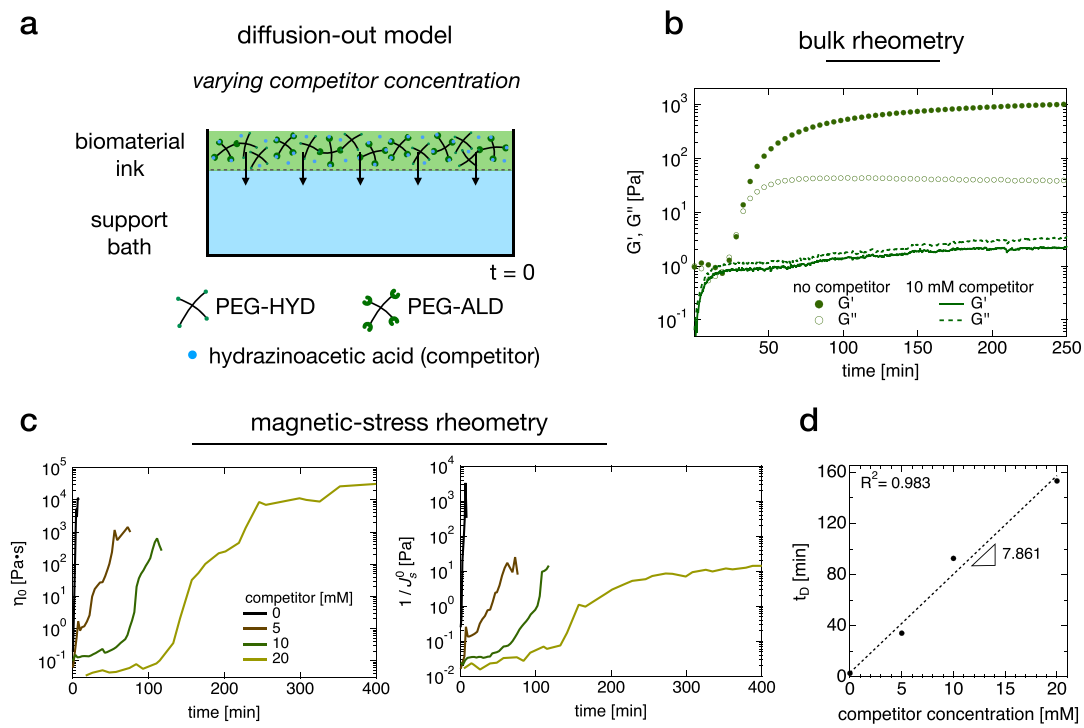

Figure 4. Gelation curves over time for dynamic PEG inks with varying competitor molecule concentration. (a) Schematic of the magnetic stress rheology setup and ink and support bath materials used for the diffusion-out model. (b) Bulk rheology measurements of the temporal evolution of G' and G'' for inks without (filled and open circular symbols, respectively) and with (solid and dashed lines, respectively) 10 mM competitor molecule premixed in the ink. The ink with the competitor remained in the sol state throughout the entire measurement ($G' < G''$). (c) Magnetic stress rheology measurements of the temporal evolution of η_0 (left) and $1/J_s^0$ (right), for 2-mm thick ink layers pre-mixed with different concentrations of the competitor, which is allowed to diffuse out of the ink over time. (d) Linear relationship between competitor molecule concentration and characteristic diffusion time t_D. The inverse of the slope of the linear regression (dashed line) corresponds to a pseudo-first-order inhibition rate constant.

rate constant of $k_i = 1/7.861 = 0.1272$ mM min$^{-1} \approx 2.12$ μM s^{-1}, with $R^2 = 0.983$. This result suggests that small-molecule inhibitors can be used not only to block gelation, but also to precisely tune the gelation rate, and provides a first-order competitor reaction model to enable such control. By incorporating known quantities of the small-molecule competitor into the ink, dynamic covalent hydrogels can be maintained in the sol state during extrusion and crosslinked after extrusion into a support bath at a rate that is optimal for both mechanical stability and cellular function. This fine tuning could be useful for multi-material printing or for applications where cells require more time to organize before the matrix stiffens [24, 60, 61]. More broadly, these results demonstrate how molecular-scale reaction and diffusion kinetics directly translate into macroscale temporal evolution of mechanical properties, as measured by the dual-layer magnetic rheometry setup.

3.4. Quantification of the effective reactant diffusivity for diffusion-out inks

We next varied the ink layer thickness to quantify the effect of different diffusion lengths in the diffusion-out system, while keeping competitor concentration constant (10 mM) (5(a)). As expected, both the normalized η_0 and $1/J_s^0$ were found to increase faster for thinner ink layers, indicating an increase in gelation kinetics due to the shorter competitor diffusion length (figure 5(b) and supplemental figure S5(b)). This behavior is consistent with a diffusion-limited crosslinking mechanism, where the rate of competitor transport into the support bath governs the rate of ink gelation.

These data were further analyzed to calculate an effective diffusivity D by plotting L^2 against t_D, as described earlier (figure 5(c)). The linear relationship suggests a Fickian diffusion model with an effective diffusivity D of 4.01×10^{-2} mm^2 min$^{-1} \approx 668$ μm^2 s^{-1}, with $R^2 = 0.888$. In previous work, the diffusivity of this competitor molecule was estimated to be ≈ 670 μm^2 s^{-1} within a similar DCC hydrogel [38]. While the two hydrogel systems are not exactly identical, the similarity in estimated diffusivity values lends confidence to the use of our magnetic rheometry setup to quantify effective diffusivity parameters. Next, we used this experimentally determined value to estimate Da for this diffusion-out ink system, similar to the procedure used above for the diffusion-in ink system (equation (4)). Here,

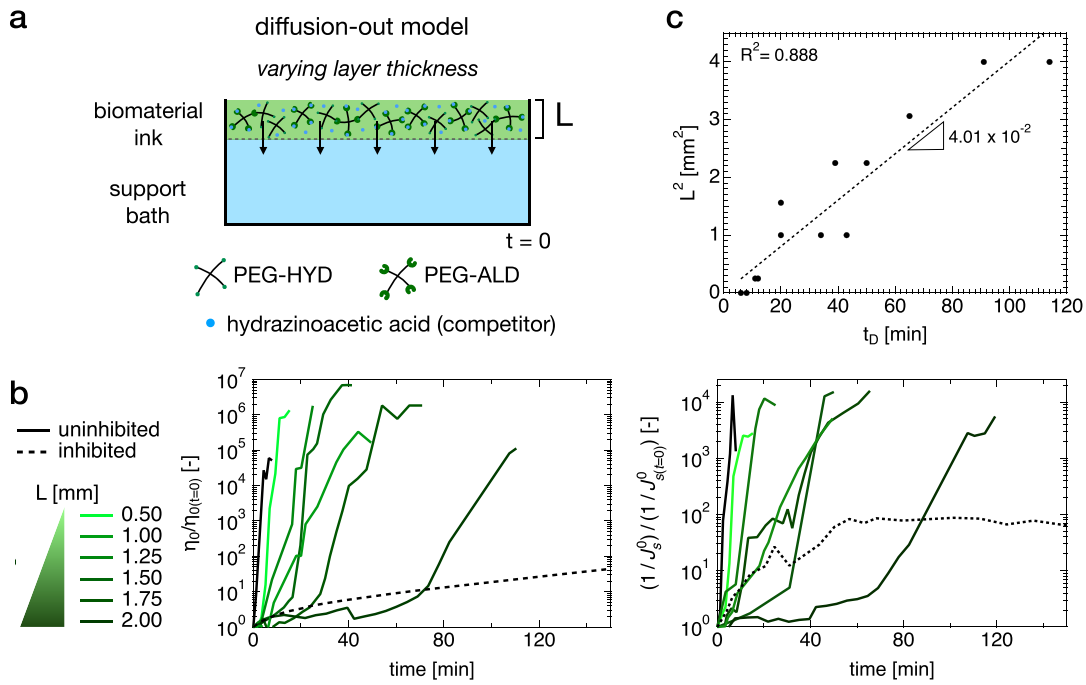

Figure 5. Dynamic PEG ink crosslinking dependence on ink layer thickness. (a) Schematic of the experimental setup with competitor diffusing from the biomaterial ink into the underlying support bath, which has different thickness L to mimic different printed filament diameters. (b) Dynamic PEG ink crosslinking for the case without competitor (i.e. uninhibited), the case with no competitor diffusion (i.e. inhibited, with competitor present also in the support bath), and for different diffusion lengths (ink layer thickness, L), presented in terms of η_0 (left) and $1/J_s^0$ (right), normalized by the initial point. (c) Correlation between L^2 and diffusion-time t_D with the linear regression (dashed line) having a slope corresponding to diffusivity.

our initial competitor concentration, c_0 was equal to 10 mM, and the reported hydrazone reaction rate, k for ALD reacting with HYD was taken to be 23 M^{-1} s^{-1} [36]. With these parameters, the range of Da spans from 8.59×10^1 to 1.37×10^3 for the ink layer thicknesses evaluated, indicating that similar to the diffusion-in system, here diffusion also dominates at the length scales studied (supplemental table S2). The critical thickness L_c at which $Da = 1$ is approximately 54 μm. This means that for 3D printing of filaments with diameters larger than 108 μm, the extent of crosslinking can be adequately predicted based on diffusion kinetics, while printing protocols for smaller filaments must primarily consider the reaction kinetics. In both the diffusion-in and the diffusion-out systems studied, the estimated critical filament diameter below which the crosslinking kinetics transition from primarily diffusion- to reaction-controlled was estimated to be 0.47 and 108 μm, respectively. Both these values are similar to or smaller than the typical filament diameters currently used in bioprinting applications, which typically range from 100 to 400 μm [44, 62]. As diffusion-enabled printing becomes more commonplace, this type of quantitative, microrheology analysis can assist with the design of printing protocols that aim to achieve more complex prints. For example, control of the diffusion-ink kinetics can enable the fabrication of constructs with finer features and the design of specimens with mechanically patterned regions to guide cell behavior.

3.5. Printing of stiffness-patterned constructs to guide cell phenotype

Next, we demonstrated a proof-of-concept application, where informed by our microrheological analysis, we fabricated hydrogels with different mechanical properties within a single construct. The mechanical properties of biological tissues are key determinants of cell function and have been shown to modulate several cellular behaviors including spreading, migration, and differentiation [63–67]. For instance, CECs alter their phenotype and migration rate in response to substrate stiffness [68–70]. Moreover, mechanosensing can be traced with translocation of specific proteins within the cell (i.e. nuclear or cytoplasmic protein localization). In particular, yes-associated protein (YAP), is a major transcriptional coactivator and crucial downstream effector of mechanosignaling that often translocates to the nuclei of cells grown on stiffer matrices [71, 72]. While many biological tissues, like the cornea, have regionalized patterns of mechanical properties, few examples of bioprinted constructs with mechanical patterns exist to date [73, 74].

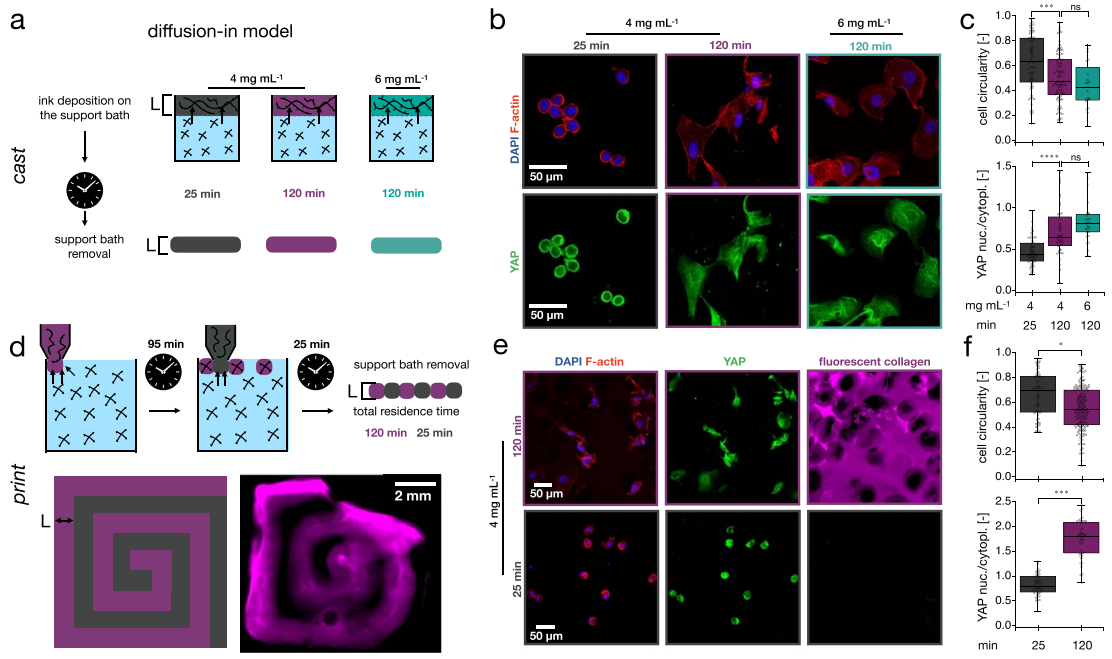

Figure 6. Fabrication of stiffness-controlled constructs to guide phenotype of human corneal epithelial cells (CECs) utilizing the diffusion-in ink model. (a) Schematic of the experimental setup where collagen-azide ink at either 4 or 6 mg ml^{-1} is deposited on the crosslinker-containing support bath (PEG-DBCO, 3 mg ml^{-1}) and allowed to crosslink for 25 or 120 min resulting in different stiffnesses. (b) Immunocytochemistry (ICC) of CECs seeded on the different cast collagen gels for the mechanoresponsive protein YAP (green) and counter-stained for cell nuclei (DAPI, blue) and cytoskeleton (F-actin, red). (c) Quantification of cell shape (top) and YAP localization (bottom) for CECs seeded on the different cast collagen gels. (d) Schematic of the experimental setup where collagen-azide ink at 4 mg ml^{-1} is 3D printed in a crosslinker-containing support bath (top). First, fluorescent-labeled collagen (magenta) was printed in a 'Greek-key' pattern. After 95 min a second pattern was printed with non-labeled collagen (gray) with an offset of 180°, and the print was allowed to crosslink for 25 more minutes (bottom left). Tilescan of the print top view after release from the support bath, showing the areas that crosslinked for longer (fluorescent collagen, pink) or shorter (non-fluorescent collagen, black) times, respectively (bottom right). (e) ICC of CECs seeded on the different areas of the print and stained for DAPI, F-actin (top), and YAP (bottom). (f) Quantification of cell shape (top) and YAP localization (bottom). (c), (f) * p <0.05, *** p <0.001,**** p <0.0001.

As a model system, we chose to explore our collagen ink utilizing the diffusion-in setup to form scaffolds for human CECs. Here, we tuned the stiffness by altering the diffusion time (i.e. residence time) and the amount of available azide groups (collagen ink concentration), both of which modulate the concentration of functional crosslinks. First, as control materials with homogeneous stiffness, we produced gels by casting a collagen ink layer (thickness, $L = 1$ mm) at a concentration of either 4 or 6 mg ml^{-1} on top of crossliker-containing support bath (PEG-DBCO, 3 mg ml^{-1}, figure 6(a)). Informed by our microrheometry characterization, the ink was allowed to crosslink through diffusion of the crosslinker from the support bath into the collagen ink for different times (25 or 120 min) in order to achieve hydrogels with different stiffnesses (figure 3(b)). For the 1 mm thick ink layer used here, 120 min is larger than the characteristic diffusion time, $t_D = 97$ min, and we assume that the hydrogel is fully crosslinked with a stiffness of ≈480 and 800 Pa for the 4 and 6 mg ml^{-1} formulations, respectively (supplemental table S1, figure 2(b)). Similarly a crosslinking time of 25 min results in a partially crosslinked hydrogel reaching approximately 5% of the final stiffness (≈25 Pa). After the respective crosslinking time had elapsed, the gels were removed from the support bath, and CECs were seeded on top of the hydrogel. After 24 h of culture, the cells were fixed and stained for the nuclei (DAPI), cytoskeleton (F-actin, phalloidin), and the mechanosensitive protein YAP (figure 6(b)). Cells seeded on 4 mg ml^{-1} collagen gels crosslinked for 25 min (i.e. softer matrices) showed a round morphology, with minimal spreading over the substrate. In contrast, the amount of spreading was significantly higher for cells grown on cast gels allowed to crosslink for 120 min (i.e. stiffer matrices), as determined both by qualitative actin visualization staining and quantitative measurement of projected 2D cell spreading (figures 6(b) and (c), top). This trend was preserved when increasing collagen concentration to 6 mg ml^{-1}, which results in a further increase in stiffness. These results align with literature showing that cells typically exhibit greater morphological spreading when grown on stiffer matrices [75]. As an indicator of active mechanosensing, we quantified the levels of nuclear translocation of the transcriptional

activator YAP. In agreement with previous research, we observed increased levels of nuclear (as compared to cytoplasmic) YAP in cells cultured on stiffer substrates (figures 6(b) and (c), bottom). As a control, CECs were additionally cultured on a stiff, glass substrate showing both a high amount of spreading and increased YAP nuclear translocation, further supporting the trends observed with our hydrogel substrates (supplemental figure S7).

After successfully fabricating gels to guide CEC phenotype by controlling gel stiffness through the diffusion time, we next sought to print a patterned hydrogel with spatial control of local stiffness. Using the same support bath, we printed 'Greek-key' patterns with high-and low-stiffness regions (figure 6(d)). We used a single collagen ink (4 mg ml^{-1}) and printed the two parts with a time difference of 95 min, resulting in a total crosslinking time of 25 and 120 min for the two different regions, similar to our aforementioned cast gel experiments. A printing nozzle with a diameter of ≈1 mm was used, and the printing took place at the top of the support bath so that diffusion of the crosslinker into the latter part of the print takes place only through a single ink-support bath interface for consistency with the earlier experiments.

Similar to the cast gels, CECs were seeded on top of these patterned constructs for 1 day prior to staining. To visualize successful patterning of the two, mechanically distinct regions, a small amount of fluorescently-labeled collagen (1:20) was added in the ink that was printed first. The print was first imaged by a slide scanner, where the presence (magenta) and absence of the fluorescence corresponds to the stiffer and softer regions, respectively (figure 6(d), bottom). At higher resolution with confocal microscopy, no fluorescent collagen was detected in the softer regions, while stiffer regions showed clear evidence of fluorescent collagen (figure 6(e)). In addition, we observed circular microstructures ($d \approx 40$ μm) in the fluorescent-labeled region, which are presumably caused by ink mixing with support bath microparticles, consistent with previous work from us and others [33, 76, 77]. In agreement with our experiments with cast gels, after 24 h we observed increased cellular spreading and significantly ($p < 0.001$) enhanced YAP nuclear translocation for the cells growing atop the stiffer regions, all within the same printed construct (figures 6(e) and (f)). These data confirm that cells within the different regions have acquired different mechanosignaling phenotypes. These results showcase the biocompatibility and mechanical versatility of our printing strategy, which uses a single ink material to achieve different printed regions with distinct mechanical properties. A further benefit of using a single ink material is its ability to enable crosslinking between the two parts without necessitating a further crosslinking step.

4. Conclusion

In 3D bioprinting, the precise control over the mechanical properties of biomaterial inks is a critical requirement due to the competing goals of printability and cytocompatibility (which typically requires softer materials) and structural stability (which requires stiffer materials). In order to achieve both of these goals, emerging technologies such as diffusion-enabled bioprinting are being designed to alter the ink viscoelastic properties over time [24]. Diffusion-enabled bioprinting typically utilizes a support bath material and small-molecule modulators to enable printability of the biomaterial ink while also facilitating post-print crosslinking into a self-supporting matrix. This can be achieved by small molecules diffusing either from the ink to the support bath (i.e. diffusion-out system) or from the support bath to the ink (i.e. diffusion-in system). In both cases, the residence time of the cell-laden ink in the support bath determines the final mechanical properties of the printed construct and hence downstream cell phenotype. A major challenge in the further development of this technology is that diffusion-driven crosslinking kinetics cannot be accurately characterized *in situ* by conventional bulk rheometry. To address this gap, here we used a custom-made magnetic rheometer utilizing a dual-layer setup to quantify viscoelastic properties over time, imitating a biomaterial ink deposited within a support bath. Moreover, compared to other microrheological techniques, such as particle tracking measurements at different depths of the ink layer, our approach is not hindered by gradual immobilization of the particles due to stiffening of the ink during crosslinking.

We demonstrate how these *in situ* rheological measurements can capture and decouple the effects of diffusion length and reaction kinetics on ink gelation behavior. We applied this approach with two hydrogel systems with opposite directions of diffusive flux, namely a collagen-based ink where a crosslinker diffuses into the ink from the support bath and a dynamic PEG ink where a competitor diffuses out of the ink into the bath. In both cases, gelation rate and final mechanical properties were distinctly influenced by diffusion length (i.e. filament radius), showing the importance of geometry in these diffusion-enabled bioprinting strategies. The ability to resolve these dynamics allowed us to extract effective diffusivities and reaction rate constants, enabling predictions of gelation for various geometries and material concentrations. Our analysis was able to predict the critical lengthscale for the crosslinking process to transition from diffusion-limited to reaction-limited through calculation of the Damköhler number. For both cases, the crosslinking kinetics were diffusion-limited for the range of ink layer thicknesses studied. The calculated critical dimensions are on the low

end of the majority of printing nozzles presently used, suggesting that the majority of diffusion-enabled bioprinting strategies currently employed are diffusion-limited, thus highlighting the importance of accurate understanding of the crosslinking timescales. These findings have practical implications for embedded 3D bioprinting, where spatial and temporal control of gelation is critical for achieving both print fidelity and control of cell phenotype. Moreover, the predicted critical lengthscale will become important as diffusion-enabled bioprinting technology is further developed to fabricate smaller features, such as vasculature with sizes ranging from 1.2 mm to 5 μm in diameter [78].

The quantitative, time-dependent analysis of bioink crosslinking enabled by magnetic rheometry also offers a powerful tool for designing printing protocols to achieve patterned constructs with regions of distinct mechanical properties. While many biological tissues and organs naturally have regions with different or alternating mechanical properties, few examples of scaffolds with alternating mechanics exist to date [79–81]. This is an important goal within biofabrication, as cells respond to matrix mechanical properties by altering their phenotype [63–67]. 3D bioprinting is uniquely positioned to achieve these regionalized structures with different local mechanical cues to induce differential cell responses, due to its ability to fabricate fine features on the multicellular lengthscale. Here, informed by our quantitative analysis of crosslinking timescales, we fabricated a specimen with patterned mechanical properties that was able to guide the phenotype of seeded human CECs. An advantage of our crosslinking strategy is the ability to fabricate hydrogel substrates with control of local stiffness values using a single biomaterial ink. This makes the printing strategy compatible with single-extrusion nozzles printers, which are currently more common than multi-nozzle printers, and also ensures strong adhesion at the interface between different regions. While here we add cells to the printed constructs after fabrication, both crosslinking chemistries used in this manuscript are cytocompatible and can be used to encapsulate cells within 3D constructs [22, 33, 82]. We previously confirmed that the presence of cells does not alter the extent of crosslinking nor the final hydrogel mechanical properties; thus, our results could be readily extended to the printing of cell-laden bioinks [22, 23]. As the library of inks and crosslinkers used for diffusive bioprinting continues to expand, our characterization and analysis techniques could be applied to other cell-compatible systems. An inherent limitation of diffusion-enabled bioprinting is the time required for ink deposition, which must be less than the diffusion time. As the ink deposition time scales linearly with the size of the construct, diffusion-enabled bioprinting is currently limited to smaller tissue constructs. Optimization of print-paths, use of multiple print-heads, or sequential fabrication of different regions would be required for larger prints [83–85]. Looking ahead, the application of this magnetic rheology technique with the Damköhler number analytical framework offers the opportunity to design and reproducibly fabricate more complex, tissue-like structures with regionalized biomechanical properties.

Acknowledgments

The authors thank C. Moose, O.B. Shende, Y. Liu, N. Eckman, M.S. Huang, and D.J. Mai for helpful technical discussions, J.D. Weiss for providing the gelatin used in the study, and the Mai lab for equipment access. We acknowledge support from the National Science Foundation (NSF), including Graduate Research Fellowship DGE-2146755 (A.S.), DMR 2103812 (S.C.H.), and DMR 2427971 (S.C.H.); the National Institutes of Health (NIH), including R01-EY035697 (S.C.H., D.M.) and F31-EY034785 (L.G.B.); the Swiss National Science Foundation Postdoc Mobility Fellowship PN-210723 (F.C.); the ARCS Foundation Scholarship (L.G.B.); the Stanford Maternal and Child Health Research Institute (MCHRI) Postdoctoral Fellowship (C.H.L.); the American Heart Association (AHA) Predoctoral Fellowship 24PRE1191604 (N.d.P.N); and the Gerald J. Lieberman Fellowship (N.d.P.N).; Japan Science and Technology Agency (JST) SPRING JPMJSP2108 (J.T.).

Data availability statement

All data that support the findings of this study are included within the article (and any supplementary files). Data have also been deposited in the Stanford Digital Repository and can be accessed through the persistent URL (https://purl.stanford.edu/hd405fx6228) and the DOI (https://doi.org/10.25740/hd405fx6228).

Supplemental Information available at https://doi.org/10.1088/1758-5090/ae7ed3/data1.

Author contributions

Fotis Christakopoulos 0000-0001-7383-5875
Conceptualization (equal), Data curation (equal), Formal analysis (equal), Investigation (equal), Methodology (equal), Validation (equal), Visualization (equal), Writing – original draft (equal), Writing – review & editing (equal)

Audrey Shih 0000-0002-8489-2178
Conceptualization (equal), Data curation (equal), Formal analysis (equal), Investigation (equal),

Methodology (equal), Software (equal), Validation (equal), Visualization (equal), Writing – original draft (equal), Writing – review & editing (equal)

Stella J Chung 0009-0001-3319-2366
Data curation (supporting), Formal analysis (supporting), Investigation (supporting), Methodology (supporting), Software (supporting), Validation (supporting), Writing – review & editing (supporting)

Carla Huerta-López 0000-0002-6943-3475
Data curation (supporting), Formal analysis (supporting), Investigation (supporting), Methodology (supporting), Visualization (supporting), Writing – review & editing (supporting)

Lucia G Brunel 0000-0003-0327-5635
Conceptualization (supporting), Investigation (supporting), Methodology (supporting), Writing – review & editing (supporting)

Narelli de Paiva Narciso 0009-0002-9249-4644
Formal analysis (supporting), Investigation (supporting), Writing – review & editing (supporting)

Clélia Messin-Roizard 0009-0006-2221-1855
Investigation (supporting), Writing – review & editing (supporting)

Junyi Tao 0009-0005-2740-1124
Investigation (supporting), Writing – review & editing (supporting)

David Myung 0000-0002-7980-3070
Funding acquisition (equal), Resources (equal), Writing – review & editing (supporting)

Sarah C Heilshorn 0000-0002-9801-6304
Conceptualization (equal), Funding acquisition (equal), Project administration (equal), Resources (equal), Supervision (equal), Visualization (equal), Writing – original draft (equal), Writing – review & editing (equal)

Gerald G Fuller 0000-0002-2924-053X
Conceptualization (equal), Funding acquisition (equal), Project administration (equal), Resources (equal), Supervision (equal), Visualization (equal), Writing – original draft (equal), Writing – review & editing (equal)

References

[1] Groll J *et al* 2016 Biofabrication: reappraising the definition of an evolving field *Biofabrication* **8** 013001
[2] Murphy S V and Atala A 2014 3D bioprinting of tissues and organs *Nat. Biotechnol.* **32** 773–85
[3] Huang M S, Christakopoulos F, Roth J G and Heilshorn S C 2025 Organoid bioprinting: from cells to functional tissues *Nat. Rev. Bioeng.* **3** 126–42
[4] Brunel L G, Hull S M and Heilshorn S C 2022 Engineered assistive materials for 3D bioprinting: support baths and sacrificial inks *Biofabrication* **14** 032001
[5] Chaudhuri O, Cooper-White J, Janmey P A, Mooney D J and Shenoy V B 2020 Effects of extracellular matrix viscoelasticity on cellular behaviour *Nature* **584** 535–46
[6] Bingcheng Y, Xu Q and Liu W 2022 An overview of substrate stiffness guided cellular response and its applications in tissue regeneration *Bioact. Mater.* **15** 82–102
[7] Willie W, DeConinck A and Lewis J A 2011 Omnidirectional printing of 3D microvascular networks *Adv. Mater.* **23** H178–83
[8] Norotte C, Marga F S, Niklason L E and Forgacs G 2009 Scaffold-free vascular tissue engineering using bioprinting *Biomaterials* **30** 5910–7
[9] Bertassoni L E *et al* 2014 Direct-write bioprinting of cell-laden methacrylated gelatin hydrogels *Biofabrication* **6** 024105
[10] Bertassoni L E *et al* 2014 Hydrogel bioprinted microchannel networks for vascularization of tissue engineering constructs *Lab Chip* **14** 2202–11
[11] Ozbolat V, Dey M, Ayan B and Ozbolat I T 2019 Extrusion-based printing of sacrificial Carbopol ink for fabrication of microfluidic devices *Biofabrication* **11** 034101
[12] Visser J, Peters B, Burger T J, Boomstra J, Dhert W J A, Melchels F P W and Malda J 2013 Biofabrication of multi-material anatomically shaped tissue constructs *Biofabrication* **5** 035007
[13] Rodrigo Pimentel C, Suk Kyu K, Caviglia C, Wolff A, Emnéus J, Keller S S and Dufva M 2018 Three-dimensional fabrication of thick and densely populated soft constructs with complex and actively perfused channel network *Acta Biomater.* **65** 174–84
[14] Miller J S *et al* 2012 Rapid casting of patterned vascular networks for perfusable engineered three-dimensional tissues *Nat. Mater.* **11** 768–74
[15] Becker M, Gurian M, Schot M and Leijten J 2023 Aqueous two-phase enabled low viscosity 3D (LoV3D) bioprinting of living matter *Adv. Sci.* **10** 2204609
[16] Sakai S and Morita T 2022 One-Step FRESH bioprinting of low-viscosity silk fibroin inks *ACS Biomater. Sci. Eng.* **8** 2589–97
[17] Tan E Y S, Suntornnond R and Yeong W Y 2021 High-resolution novel indirect bioprinting of low-viscosity cell-laden hydrogels via model-support bioink interaction *3D Print. and Addit. Manuf.* **8** 69–78
[18] Highley C B, Rodell C B and Burdick J A 2015 Direct 3D printing of shear-thinning hydrogels into self-healing hydrogels *Adv. Mater. (Deerfield Beach, Fla.)* **27** 5075–9
[19] Hinton T J, Jallerat Q, Palchesko R N, Park J H, Grodzicki M S, Shue H-J, Ramadan M H, Hudson A R and Feinberg A W 2015 Three-dimensional printing of complex biological structures by freeform reversible embedding of suspended hydrogels *Sci. Adv.* **1** e1500758
[20] Ying G-L, Jiang N, Maharjan S, Yin Y-X, Chai R-R, Cao X, Yang J-Z, Miri A K, Hassan S and Zhang Y S 2018 Aqueous two-phase emulsion bioink-enabled 3D bioprinting of porous hydrogels *Adv. Mater.* **30** 1805460
[21] Bhattacharjee T, Zehnder S M, Rowe K G, Jain S, Ryan M N, Sawyer W G and Angelini T E 2015 Writing in the granular gel medium *Sci. Adv.* **1** e1500655
[22] Hull S M, Lindsay C D, Brunel L G, Shiwarski D J, Tashman J W, Roth J G, Myung D, Feinberg A W and Heilshorn S C 2021 3D bioprinting using universal orthogonal network (UNION) bioinks *Adv. Funct. Mater.* **31** 2007983
[23] Hull S M, Lou J, Lindsay C D, Navarro R S, Cai B, Brunel L G, Westerfield A D, Xia Y and Heilshorn S C 2023 3D bioprinting of dynamic hydrogel bioinks enabled by small molecule modulators *Sci. Adv.* **9** eade7880

[24] Cai B, Kilian D, Mejia D R, Rios R J, Ali A and Heilshorn S C 2024 Diffusion-based 3D bioprinting strategies *Adv. Sci.* **11** 2306470
[25] Lindsay C D, Roth J G, LeSavage B L and Heilshorn S C 2019 Bioprinting of stem cell expansion lattices *Acta Biomater.* **95** 225–35
[26] Palma J H, Bertuola M and Hermida Elida B 2024 Modeling calcium diffusion and crosslinking dynamics in a thermo-gelling alginate-gelatin-hyaluronic acid ink: 3d bioprinting applications *Bioprinting* **38** e00329
[27] Shin S, Brunel L G, Cai B, Kilian D, Roth J G, Seymour A J and Heilshorn S C 2023 Gelation of uniform interfacial diffusant in embedded 3D printing *Adv. Funct. Mater.* **33** 2307435
[28] Shih A, Chung S J, Shende O B, Herwald S E, Vezeridis A M and Fuller G G 2024 Viscoelastic measurements of abscess fluids using a magnetic stress rheometer *Phys. Fluids* **36** 111919
[29] Cai P C, Braunreuther M, Shih A, Spakowitz A J, Fuller G G and Heilshorn S C 2024 Air-liquid intestinal cell culture allows in situ rheological characterization of intestinal mucus *APL Bioeng.* **8** 026112
[30] Braunreuther M, Arenhoevel J, Bej R, Moose C, Mall M A, Haag R and Fuller G G 2025 Magnetic microwire rheometer reveals differences in hydrogel degradation via disulfide reducing agents *Soft Matter* **21** 427–34
[31] Braunreuther M, Liegeois M, Fahy J V and Fuller G G 2023 Nondestructive rheological measurements of biomaterials with a magnetic microwire rheometer *J. Rheol.* **67** 579–88
[32] DeForest C A, Polizzotti B D and Anseth K S 2009 Sequential click reactions for synthesizing and patterning three-dimensional cell microenvironments *Nat. Mater.* **8** 659–64
[33] Brunel L G, Christakopoulos F, Kilian D, Cai B, Hull S M, Myung D and Heilshorn S C 2024 Embedded 3D bioprinting of collagen inks into microgel baths to control hydrogel microstructure and cell spreading *Adv. Healthcare Mater.* **13** 2303325
[34] Brunel L G *et al* 2025 Reinforcement of fibrillar collagen hydrogels with bioorthogonal covalent crosslinks *Biomacromolecules* **26** 4404–18
[35] Brunel L G, Cai B, Hull S M, Han U, Wungcharoen T, Fernandes-Cunha G M, Seo Y A, Johansson P K, Heilshorn S C and Myung D 2025 In situ universal orthogonal network (union) bioink deposition for direct delivery of corneal stromal stem cells to corneal wounds *Bioact. Mater.* **48** 414–30
[36] McKinnon D D, Domaille D W, Cha J N and Anseth K S 2014 Biophysically defined and cytocompatible covalently adaptable networks as viscoelastic 3d cell culture systems *Adv. Mater.* **26** 865–72
[37] Lou J and Xia Y 2022 Using competitor molecules to reversibly modulate the mechanical properties of viscoelastic hydrogels *ACS Macro Lett.* **11** 1312–6
[38] Gilchrist A E, Liu Y, Klett K, Liu Y-C, Ceva S and Heilshorn S C 2023 Transient competitors to modulate dynamic covalent cross-linking of recombinant hydrogels *Chem. Mater.* **35** 8969–83
[39] Liu Y *et al* 2025 Engineered hydrogels for organoid models of human nonalcoholic fatty liver disease *Adv. Sci.* **12** e17332
[40] Lee H J, Fernandes-Cunha G M, Kyung-Sun N, Hull S M and Myung D 2018 Bio-orthogonally crosslinked, in situ forming corneal stromal tissue substitute *Adv. Healthcare Mater.* **7** 1800560
[41] Brunel L G, Long C M, Christakopoulos F, Cai B, Johansson P K, Singhal D, Enejder A, Myung D and Heilshorn S C 2025 Interpenetrating networks of fibrillar and amorphous collagen promote cell spreading and hydrogel stability *Acta Biomater.* **193** 128–42
[42] Jönsson P, Jonsson M P, Tegenfeldt J O and Höök F 2008 A method improving the accuracy of fluorescence recovery after photobleaching analysis *Biophys. J.* **95** 5334–48
[43] McCauley P J, Fromen C A and Bayles A V 2025 Cell viability in extrusion bioprinting: the impact of process parameters, bioink rheology and cell mechanics *Rheol. Acta* **64** 497–515
[44] Schwab A, Levato R, D'Este M, Piluso S, Eglin D and Malda J 2020 Printability and shape fidelity of bioinks in 3d bioprinting *Chem. Rev.* **10** 11028–55
[45] Pottathara Y B and Kokol V 2023 Effect of nozzle diameter and cross-linking on the micro-structure, compressive and biodegradation properties of 3d printed gelatin/collagen/hydroxyapatite hydrogel *Bioprinting* **31** e00266
[46] Morrison F A 2001 *Understanding Rheology* (*Topics in Chemical Engineering*) (Oxford University Press)
[47] Singhal D, Christakopoulos F, Brunel L G, Borkar S, Doulames V M, Mozipo E A T, Myung D, Fuller G G and Heilshorn S C 2026 Dual-orientation of collagen fibers to guide cell alignment in 3d-printed constructs *Acta Biomater.* **209** 167–82
[48] Engler A J, Sen S, Sweeney H L and Dennis E D 2006 Matrix elasticity directs stem cell lineage specification *Cell* **126** 677–89
[49] Saha K, Keung A J, Irwin E F, Li Y, Little L, Schaffer D V and Healy K E 2008 Substrate modulus directs neural stem cell behavior *Biophys. J.* **95** 4426–38
[50] Xiaowei Li *et al* 2019 Nanofiber-hydrogel composite-mediated angiogenesis for soft tissue reconstruction *Sci. Transl. Med* **11** 6210
[51] Kizilay M Y and Okay O 2003 Effect of hydrolysis on spatial inhomogeneity in poly(acrylamide) gels of various crosslink densities *Polymer* **44** 5239–50
[52] Deforest C A, Sims E A and Anseth K S 2010 Peptide-functionalized click hydrogels with independently tunable mechanics and chemical functionality for 3d cell culture *Chem. Mater.* **22** 4783–90
[53] de Paiva Narciso N, Navarro R S, Gilchrist A E, Trigo M L M, Rodriguez G A and Heilshorn S C 2023 Design parameters for injectable biopolymeric hydrogels with dynamic covalent chemistry crosslinks *Adv. Healthcare Mater.* **12** 2301265
[54] Shigehara O Toshiro M and Keishi K 1970 Rheological properties of anionic polystyrenes. i. dynamic viscoelasticity of narrow-distribution polystyrenes *Macromolecules* **3** 116
[55] Dealy J M, Read D J and Larson R G 2006 *Structure and Rheology of Molten Polymers* (Carl Hanser Verlag GmbH & Co)
[56] Fogler S H 2016 *Elements of Chemical Reaction Engineering* 5th edn (Pearson Education)
[57] Dommerholt J, Rutjes F P J T and Van Delft F L 2016 Strain-promoted 1,3-dipolar cycloaddition of cycloalkynes and organic azides *Top. Curr. Chem.* **374** 16
[58] Runze X, Ooi H S, Bian L, Ouyang L and Sun W 2025 Dynamic hydrogels for biofabrication: a review *Biomaterials* **320** 123266
[59] Wei Long N, Vyas C, Huang B, Yeong W Y and Bartolo P 2025 Advanced bioprinting strategies for fabrication of biomimetic tissues and organs *Int. J. Extrem. Manuf.* **7** 062006
[60] Dikyol C, Altunbek M, Bartolo P and Koc B 2021 Multimaterial bioprinting approaches and their implementations for vascular and vascularized tissues *Bioprinting* **24** e00159
[61] Yuan Z *et al* 2025 Multimaterial and multidimensional bioprinting in regenerative medicine: Advances, limitations and future directions *Adv. Healthcare Mater.* **14** 2500475
[62] Zhang Y S, Haghiashtiani G, Hübscher T, Kelly D J, Lee J M, Lutolf M, McAlpine M C, Yeong W Y, Zenobi-Wong M and Malda J 2021 3d extrusion bioprinting *Nat. Rev. Methods Primers* **1** 75
[63] Cheng N *et al* 2022 Hydrogel platform capable of molecularly resolved pulling on cells for mechanotransduction *Mater. Today Bio* **17** 100476

[64] Hachet E, Berghe H V D, Bayma E, Block M R and Auzely-Velty R 2012 Design of biomimetic cell-interactive substrates using hyaluronic acid hydrogels with tunable mechanical properties *Biomacromolecules* **13** 1818–27
[65] Hunt D R *et al* 2021 Engineered matrices enable the culture of human patient-derived intestinal organoids *Adv. Sci.* **8** 2004705
[66] Darnell M, Young S, Luo G, Shah N, Lippens E, Weaver J, Duda G and Mooney D 2017 Substrate stress-relaxation regulates scaffold remodeling and bone formation in vivo *Adv. Healthcare Mater.* **6** 1601185
[67] Navarro R S, Huang M S, Roth J G, Hubka K M, Long C M, Enejder A and Heilshorn S C 2022 Tuning polymer hydrophilicity to regulate gel mechanics and encapsulated cell morphology *Adv. Healthcare Mater.* **11** e2200011
[68] Molladavoodi S, Kwon H J, Medley J and Gorbet M 2015 Human corneal epithelial cell response to substrate stiffness *Acta Biomater.* **11** 324–32
[69] Gouveia R M, Lepert G, Gupta S, Mohan R R, Paterson C and Connon C J 2019 Assessment of corneal substrate biomechanics and its effect on epithelial stem cell maintenance and differentiation *Nat. Commun.* **10** 1496
[70] Masterton S and Ahearne M 2019 Influence of polydimethylsiloxane substrate stiffness on corneal epithelial cells *R. Soc. Open Sci.* **6** 191796
[71] Stanton A E, Tong X and Yang F 2019 Extracellular matrix type modulates mechanotransduction of stem cells *Acta Biomater.* **96** 310–20
[72] Scott K E, Fraley S I and Rangamani P 2021 A spatial model of YAP/TAZ signaling reveals how stiffness, dimensionality and shape contribute to emergent outcomes *Proc. Natl Acad. Sci.* **118** e2021571118
[73] Blackburn B J, Jenkins M W, Rollins A M and Dupps W J 2019 A review of structural and biomechanical changes in the cornea in aging, disease and photochemical crosslinking *Front. Bioeng. Biotechnol.* **7** 66
[74] Formisano N, van der Putten C, Grant R, Sahin G, Truckenmüller R K, Bouten C V C, Kurniawan N A and Giselbrecht S 2021 Mechanical properties of bioengineered corneal stroma *Adv. Healthcare Mater.* **10** 2100972
[75] Discher D E, Janmey P and Wang Y-Li 2005 Tissue cells feel and respond to the stiffness of their substrate *Science* **310** 1139–43
[76] Lee A, Hudson A R, Shiwarski D J, Tashman J W, Hinton T J, Yerneni S, Bliley J M, Campbell P G and Feinberg A W 2019 3d bioprinting of collagen to rebuild components of the human heart *Science* **365** 482–7
[77] Friedrich L M, Gunther R T and Seppala J E 2022 Suppression of filament defects in embedded 3d printing *ACS Appl. Mater. Interfaces* **14** 32561–78
[78] Sexton Z A *et al* 2025 Rapid model-guided design of organ-scale synthetic vasculature for biomanufacturing *Science* **388** 1198–204
[79] Matsuzaki T *et al* 2023 Preparation of mechanically patterned hydrogels for controlling the self-condensation of cells *STAR Protocols* **4** 102471
[80] Cui J, Ruisheng X, Dong W, Kaneko T, Chen M and Shi D 2023 Skin-inspired patterned hydrogel with strain-stiffening capability for strain sensors *ACS Appl. Mater. Interfaces* **15** 48736–43
[81] Liu B *et al* 2024 4d printed hydrogel scaffold with swelling-stiffening properties and programmable deformation for minimally invasive implantation *Nat. Commun.* **15** 1587
[82] Huang M S, LeSavage B L, Ghorbani S, Gilchrist A E, Roth J G, Huerta-López C, Mozipo E A, Navarro R S and Heilshorn S C 2025 Viscoelastic n-cadherin-like interactions maintain neural progenitor cell stemness within 3d matrices *Nat. Commun.* **16** 5213
[83] Phung L X, Tuan Quang T, Pham V H, Nguyen M T H, Truong D and Nguyen T K 2024 The development of a modular and open-source multi-head 3d bioprinter for fabricating complex structures *Bioprinting* **39** e00339
[84] Ravanbakhsh H, Karamzadeh V, Bao G, Mongeau L, Juncker D and Zhang Y S 2021 Emerging technologies in multi-material bioprinting *Adv. Mater.* **33** e2104730
[85] Claire Y *et al* 2020 A sequential 3d bioprinting and orthogonal bioconjugation approach for precision tissue engineering *Biomaterials* **258** 120294